

# Theranostic Unimolecular Micelles Based on Brush-Shaped Amphiphilic Block Copolymers for Tumor-Targeted Drug Delivery and Positron Emission Tomography Imaging

Jintang Guo,<sup>†,‡,§,⊥</sup> Hao Hong,<sup>†,#</sup> Guojun Chen,<sup>⊥,||</sup> Sixiang Shi,<sup>||</sup> Tapas R. Nayak,<sup>#</sup> Charles P. Theuer,<sup>△</sup> Todd E. Barnhart,<sup>#</sup> Weibo Cai,<sup>\*,#,||</sup> and Shaoqin Gong<sup>\*,§,⊥,||</sup>

<sup>†</sup> School of Chemical Engineering, Tianjin University, Tianjin 300072, China

<sup>§</sup> Department of Biomedical Engineering, University of Wisconsin–Madison, Madison, Wisconsin 53706, United States

<sup>⊥</sup> Wisconsin Institutes for Discovery, University of Wisconsin–Madison, Madison, Wisconsin 53715, United States

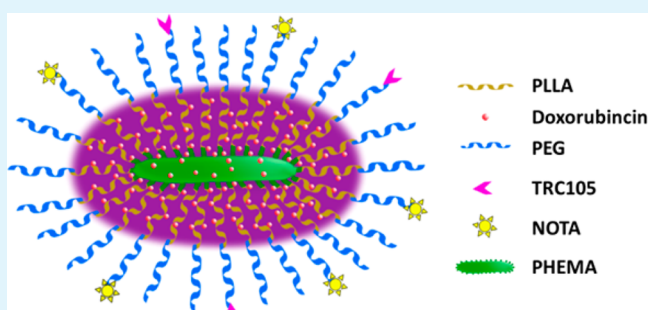
<sup>#</sup> Departments of Radiology and Medical Physics, University of Wisconsin–Madison, Madison, Wisconsin 53705, United States

<sup>||</sup> Materials Science Program, University of Wisconsin–Madison, Madison, Wisconsin 53706, United States

<sup>△</sup> TRACON Pharmaceuticals, Inc., San Diego, California, United States

**ABSTRACT:** Brush-shaped amphiphilic block copolymers were conjugated with a monoclonal antibody against CD105 (i.e., TRC105) and a macrocyclic chelator for <sup>64</sup>Cu-labeling to generate multifunctional theranostic unimolecular micelles. The backbone of the brush-shaped amphiphilic block copolymer was poly(2-hydroxyethyl methacrylate) (PHEMA) and the side chains were poly(L-lactide)-poly(ethylene glycol) (PLLA-PEG). The doxorubicin (DOX)-loaded unimolecular micelles showed a pH-dependent drug release profile and a uniform size distribution. A significantly higher cellular uptake of TRC105-conjugated micelles was observed in CD105-positive human umbilical vein endothelial cells (HUVEC) than nontargeted micelles due to CD105-mediated endocytosis. In contrast, similar and extremely low cellular uptake of both targeted and nontargeted micelles was observed in MCF-7 human breast cancer cells (CD105-negative). The difference between the *in vivo* tumor accumulation of <sup>64</sup>Cu-labeled TRC105-conjugated micelles and that of nontargeted micelles was studied in 4T1 murine breast tumor-bearing mice, by serial positron emission tomography (PET) imaging and validated by biodistribution studies. These multifunctional unimolecular micelles offer pH-responsive drug release, noninvasive PET imaging capability, together with both passive and active tumor-targeting abilities, thus making them a desirable nanoplatform for cancer theranostics.

**KEYWORDS:** brush polymer, unimolecular micelles, nanocarriers, brush-shaped amphiphilic block copolymer, cancer, theranostics, CD105, angiogenesis, positron emission tomography (PET), <sup>64</sup>Cu



## INTRODUCTION

Theranostics, a treatment strategy that combines therapeutics with diagnostics, can increase drug efficacy and safety as well as allow for therapeutic response monitoring.<sup>1,2</sup> Theranostics has been actively studied in recent years because it can pave the road for personalized medicine. Nanotechnology can offer unprecedented opportunities for the design of these agents, where the diagnostic component can be used not only before and after but also throughout the treatment regimen.<sup>3–5</sup>

Among the many imaging techniques, positron emission tomography (PET) is highly attractive because it possesses many desirable features for potential clinical translation, such as noninvasiveness, very high sensitivity, tomographic in nature, unlimited tissue penetration of signal, capability for accurate quantitation of signal, and widespread use in clinical oncology.<sup>6</sup> In the field of nanomedicine, drug nanocarriers engineered with

proper isotope chelators can be labeled with desirable isotopes such as <sup>64</sup>Cu ( $t_{1/2}$ : 12.7 h). The tumor-targeting efficacy, *in vivo* biodistribution, and pharmacokinetics of the <sup>64</sup>Cu-labeled nanocarriers can then be quantitatively and noninvasively evaluated using PET.<sup>7,8</sup> Such theranostic nanomedicine will enable physicians to evaluate the therapeutic outcome and closely monitor cancer progression/regression in individual patients, thus facilitating more effective and personalized cancer patient management. The application of such targeted cancer

**Special Issue:** Materials for Theranostics

**Received:** January 13, 2014

**Accepted:** March 4, 2014

**Published:** March 14, 2014

theranostics in clinical practice may start a new era of cancer diagnosis and therapy.

Polymer micelles self-assembled from amphiphilic block copolymers have been extensively studied due to the flexibility in controlling their physical, chemical, and biological properties.<sup>9</sup> However, conventional multimolecular micelles tend to exhibit insufficient in vivo stability because of the influence of multiple factors including the polymer concentration, serum protein–micelle interactions, temperature, flow stress, and ionic strength.<sup>9</sup> For example, when the polymer concentration is below its critical micelle concentration, the multimolecular polymer micelles disassemble. This will then lead to a rapid release of the payload in the bloodstream, which can cause systemic toxicity and loss of the disease-targeting capability provided by the drug nanocarriers. To overcome such thermodynamic instability, researchers have investigated various strategies, such as cross-linking the core or shell or both,<sup>10</sup> and the development of unimolecular micelles.<sup>7</sup> Unimolecular micelles have a core–shell structure, which topologically resembles multimolecular polymeric micelles; however, unimolecular micelles can maintain excellent micellar stability because they are formed by individual multiarm amphiphilic block copolymer molecules consisting of only covalent bonds. Compared with the cross-linking strategy, unimolecular micelles can provide excellent in vivo stability without compromising their biodegradability or drug release profiles.<sup>11,12</sup>

The size of unimolecular micelles can be easily controlled by adjusting the molecular weights of the hydrophilic and hydrophobic segments, and the number of the amphiphilic block copolymer arms.<sup>13,14</sup> The morphology of micelles can significantly alter their behaviors in biological organisms and cells. For example, a previous study reported that worm-like polymer micelles formed by amphiphilic PEG–polycaprolactone block copolymers showed a longer circulation time as compared to their spherical counterparts.<sup>15,16</sup> While unimolecular micelles formed by spherical multiarm star amphiphilic block copolymers have been well studied for drug delivery applications,<sup>17–22</sup> unimolecular micelles formed by brush-shaped amphiphilic block copolymers are understudied for targeted drug delivery.<sup>23,24</sup> In this work, we report the development of a new type of unimolecular micelle formed by brush-shaped amphiphilic block copolymers that incorporates anticancer drug, active tumor-targeting ligand, and diagnostic PET imaging capabilities.

CD105 (also named endoglin) was chosen as the target of interest in this study, which is primarily expressed on proliferating endothelial cells and a widely accepted marker for tumor angiogenesis.<sup>25</sup> Because the expression levels of CD105 correlate adversely with prognosis in multiple cancer types, it offers enormous clinical applicability as a prognostic, diagnostic, and therapeutic vascular target in cancer.<sup>26</sup> TRC105, which is a human/murine chimeric IgG1 monoclonal antibody (mAb), exhibited high avidity for in vivo targeting and noninvasive imaging of CD105 in a number of preclinical tumor models.<sup>27–32</sup> A multicenter phase I trial of TRC105 has been reported and multiple phase II trials are ongoing in cancer patients of various tumor types.<sup>33</sup> These encouraging bench and bedside data support the further development of TRC105-based nanomedicine, which can play key roles in future cancer patient care.

In this work, multifunctional unimolecular micelles formed by brush-shaped amphiphilic poly(2-hydroxyethyl methacry-

late) (PHEMA)-poly(L-lactide) (PLLA)-poly(ethylene glycol) (PEG) block copolymer conjugated with TRC105 and 1,4,7-triazacyclononane-N, N',N-triacetic acid (NOTA, a macrocyclic chelator for <sup>64</sup>Cu) (PHEMA-PLLA-PEG-TRC105) were synthesized and evaluated for cancer-targeted drug delivery, which could be noninvasively measured via PET imaging (Figure 1). The CD105-targeting efficiency of these micelles

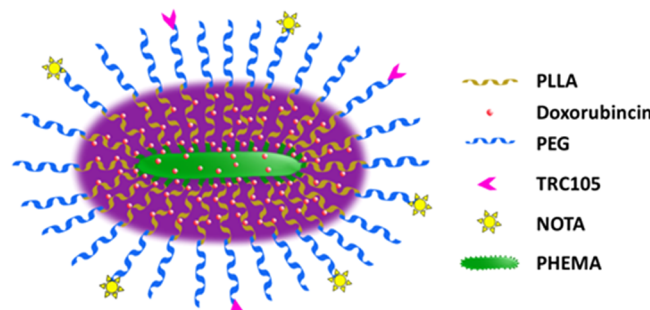


**Figure 1.** Schematic illustration of the multifunctional unimolecular micelles with TRC105 as the targeting ligand.

was studied in both CD105-positive human umbilical vein endothelial cells (HUVEC) and CD105-negative MCF-7 human breast cancer cells. To evaluate the in vivo tumor targeting efficacy, in vivo biodistribution, and pharmacokinetics of these unimolecular micelles in 4T1 murine breast tumor-bearing mice, serial PET imaging was conducted after the micelles were labeled with <sup>64</sup>Cu.

## EXPERIMENTAL SECTION

**Chemicals.** The material 2-hydroxyethyl methacrylate (HEMA; ACROS, Fair Lawn, NJ, USA) was dried over molecular sieves (type 4A) for 24 h followed by distillation under low pressure. Ethyl 2-bromo isobutyrate (EBiB), 2,2-bipyridine (bipy), cupric bromide (CuBr<sub>2</sub>), tetrahydrofuran (THF), anhydrous dichloromethane (DCM), anhydrous dimethyl sulfoxide (DMSO), triethylamine (TEA), anhydrous dimethylformamide (DMF), tannous (II) octoate (Sn(Oct)<sub>2</sub>), tris(2-carboxyethyl)phosphine (TCEP), 2-butanone, and L-lactide (LLA) were all purchased from Sigma–Aldrich Corporation (Milwaukee, WI, USA). The material 2-butanone was dried over molecular sieves (type 4A) for 24 h and L-lactide (LLA) was recrystallized twice from ethyl acetate before use. Carboxylic-PEG-maleimide (HOOC-PEG-Mal, 5000 g/mol), and carboxylic-PEG-methoxy (HOOC-PEG-methoxy, 5000 g/mol) were purchased from JenKem Technology (Allen, TX, USA). Cuprous bromide (CuBr), calcium hydride (CaH<sub>2</sub>), 4-dimethylamino pyridine (DMAP), amino-ethanethiol hydrochloride (AET-HCl), and 1,3-dicyclohexylcarbodiimide (DCC) were obtained from ACROS and used as received. Methanol was dried over CaH<sub>2</sub> and distilled prior to use. The agents 2-iminothiolane (Traut's reagent) and 5,5'-dithio-bis-(2-nitrobenzoic acid) (Ellman's reagent) were acquired from Thermo Scientific (Rockford, IL, USA). (S)-2-(4-isothiocyanatobenzyl)-1,4,7-triazacyclononane-1,4,7-triacetic acid (abbreviated as p-SCN-Bn-NOTA) was purchased from Macrocyclics (Dallas, TX, USA). Doxorubicin hydrochloride (DOX-HCl) was procured from Beijing Mesocom Technology Co., Ltd. (Beijing, China). TRC105 was provided by TRACON Pharmaceuticals (San Diego, CA, USA). All other chemicals and reagents used were of analytical reagent grade. The buffers were of Millipore grade and pretreated with Chelex 100 resin (50–100 mesh, Sigma–Aldrich, St. Louis, MO, USA).

**Characterization.** The <sup>1</sup>H NMR spectra were measured by a Varian Mercury Plus 300 spectrometer using DMSO-d<sub>6</sub> or CDCl<sub>3</sub>-d as a solvent at 25 °C. The IR spectra of all polymer samples were measured using Bruker Tensor 27 FT-IR. The number average molecular weight (M<sub>n</sub>) and polydispersity index (PDI) of the polymers

were determined by a Viscotek GPC system (Malvern Instruments, Westborough, MA, USA) equipped with triple detectors (i.e., refractive index, viscometer, and a light scattering detectors) using DMF as an eluent at a flow rate of 1.0 mL/min. PMMA with a narrow polydispersity was used as the calibration standard. The size distribution of the unimolecular micelles (0.05 mg/mL) were analyzed by dynamic light scattering (DLS) using a Malvern ZetaSizer Nano ZS90 system (Malvern Instruments, USA). The morphology of the dried unimolecular micelles were determined using a FEI Tecnai G<sup>2</sup> F30 TWIN transmission electron microscope (TEM; 300 kV, E.A. Fischione Instruments, Inc. USA). TEM samples were prepared by depositing a drop of micelle solution (0.05 mg/mL) containing 1 wt % of phosphotungstic acid onto a 200 mesh copper grid coated with carbon and dried at room temperature. The DOX loading level was measured by a UV-visible spectrophotometer (Varian Cary 300 Bio, Agilent Technologies) based on DOX's absorbance at 485 nm.

**Synthesis of PHEMA.** PHEMA was synthesized by atom transfer radical polymerization (ATRP) using EBiB as an initiator and CuBr/2,2-bipyridine (bipy) as a catalyst. Solutions of CuBr (7.56 mg,  $5.27 \times 10^{-5}$  mol), EBiB (12.86 mg,  $6.59 \times 10^{-5}$  mol), 2,2-bipyridine (20.60 mg,  $1.32 \times 10^{-4}$  mol), CuBr<sub>2</sub> (2.95 mg,  $1.32 \times 10^{-5}$  mol), and HEMA (4 mL, 0.033 mol) in a 12 mL solvent mixture of 2-butatone and methanol (2:1 by volume) were prepared with a molar ratio of 0.8:1.2:0.2:500. The solutions were thoroughly deoxygenated under an argon atmosphere and the reaction was proceeded for 5 h at 50 °C. The obtained crude product was diluted by methanol and passed through a silica gel column to remove the copper catalyst. The final product was obtained by precipitation in THF. It was then dried in a vacuum oven for 48 h at room temperature to yield a white powder.  $M_n$ <sub>GPC</sub> = 12 510,  $M_w/M_n$  = 1.379. IR (cm<sup>-1</sup>): 3360 (ν<sub>O-H</sub>), 2945 (ν<sub>C-H</sub>), 1720 (ν<sub>C=O</sub>). <sup>1</sup>H NMR (DMSO-d<sub>6</sub>, δ, ppm): 4.78 (s, OH), 3.88 (m, COOCH<sub>2</sub>), 3.58 (m, CH<sub>2</sub>OH), 1.74 (m, CH<sub>2</sub>), 0.76 (m, CH<sub>3</sub>).

**Synthesis of PHEMA-PLLA.** PHEMA-PLLA was synthesized by ring-opening polymerization (ROP) of L-lactide using Sn(Oct)<sub>2</sub> as a catalyst. A 50 mL Schlenk flask was loaded with PHEMA (350 mg,  $2.80 \times 10^{-5}$  mol) and 5 mL of anhydrous DMF before a predetermined amount of L-lactide (5.82 g, 40.42 mmol) was introduced under an argon atmosphere. After the dissolution of PHEMA and L-lactide, a catalytic amount of Sn(Oct)<sub>2</sub> ([Sn(Oct)<sub>2</sub>]/[monomer] = 1:1000) was added. The reaction was carried out in an oil bath at 120 °C for 24 h. After being cooled to room temperature, the mixture was diluted with THF and precipitated into cold methanol. The final product was dried under vacuum to give a white powder.  $M_n$ <sub>GPC</sub> = 73 662,  $M_w/M_n$  = 1.328. IR (cm<sup>-1</sup>): 2989 (ν<sub>C-H</sub>), 1752 (ν<sub>C=O</sub>), 1090 (ν<sub>C-O-C</sub>). <sup>1</sup>H NMR (DMSO-d<sub>6</sub>, δ, ppm): 5.17 (m, C(O)CH(CH<sub>3</sub>)O) in PLLA), 4.18 (m, C(O)CH(CH<sub>3</sub>)OH in PLLA), 1.46 (d, C(O)CH(CH<sub>3</sub>)O), 1.27 (d, C(O)CH(CH<sub>3</sub>)OH).

**Synthesis of PHEMA-PLLA-PEG-methoxy/Mal.** The coupling reaction was conducted in anhydrous DCM in the presence of DMAP and DCC. HOOC-PEG-Mal (35.5 mg,  $7.11 \times 10^{-6}$  mol, maleimide content: 70% in molar), HOOC-PEG-methoxyl (46.2 mg,  $9.24 \times 10^{-6}$  mol), and DCC (3.37 mg,  $1.64 \times 10^{-5}$  mol) were loaded into a 50 mL two-necked flask. The mixture was vacuumed for 1 h followed by argon exchange three times. After 10 mL of anhydrous DCM was added, the mixture was reacted for 30 min under stirring. PHEMA-PLLA (30 mg) and DMAP (0.20 mg,  $1.63 \times 10^{-6}$  mol) were added into the reaction system, which was allowed to react for 20 h under an argon atmosphere. After removal of dicyclohexylurea (DCU), a crude product was obtained through precipitation in cold ethyl ether. The impurities were removed through dialysis against DI water using a cellulose dialysis membrane (molecular weight cutoff [MWCO] of 15 kDa) for 48 h. Finally, the polymer was dried by lyophilization.  $M_n$ <sub>GPC</sub> = 355 580,  $M_w/M_n$  = 1.472. IR (cm<sup>-1</sup>): 2883 (ν<sub>C-H</sub>), 1750 (ν<sub>C=O</sub>), 1090 (ν<sub>C-O-C</sub>). <sup>1</sup>H NMR (CDCl<sub>3</sub>-d, δ, ppm): 6.68 (C(O)CH=CHC(O)), 5.17 (m, C(O)CH(CH<sub>3</sub>)O) in PLLA), 3.67 (m, CH<sub>2</sub> in PEG), 3.4 (s, OCH<sub>3</sub> in PEG), 1.46 (d, CH<sub>3</sub> in PLLA).

**Synthesis of Brush-Shaped Amphiphilic PHEMA-PLLA-PEG-methoxy/TRC105/NOTA Block Copolymers.** NOTA-SH was prepared via a reaction between p-SCN-Bn-NOTA (2.8 mg, 0.005

mmol) and AET·HCl (0.57 mg, 0.005 mmol) conducted in 1 mL PBS under nitrogen for 2 h.<sup>8</sup> The reaction of TRC105 and Traut's reagent (molar ratio = 1:20) was carried out in PBS (pH 8.0) for 2 h. After the reaction was complete, TRC105-SH was purified by size exclusion chromatography using PBS as the mobile phase. A fixed amount of TRC105-SH and NOTA-SH solutions were added into the PHEMA-PLLA-PEG-methoxy/Mal suspension in PBS (pH 7.5) with a molar ratio of TRC105, NOTA, and PHEMA-PLLA-PEG-methoxy/Mal at 8:11:1. TCEP was also added into the reaction system to avoid the potential formation of disulfide bonds between TRC105-SH and NOTA-SH, or among themselves. The impurities were removed by centrifugation filtration using 30 kDa cutoff Amicon filters. The resulting final product, abbreviated as PHEMA-PLLA-PEG-TRC105, was used to prepare targeted unimolecular micelles. Brush-shaped amphiphilic block copolymers without TRC105 conjugation synthesized using a similar procedure, were used to prepare nontargeted unimolecular micelles.

**Preparation of Drug-Loaded Unimolecular Micelles.** Ten milligrams of the targeted or nontargeted brush-shaped amphiphilic block copolymers and 4 mg of DOX-HCl were dissolved in a 5 mL DMF solution under stirring, with the pH value adjusted to 7.0 using a TEA solution. After 2 h of reaction, 15 mL of DI water was added dropwise to the solution. After 18 h, the mixture was dialyzed against DI water using a dialysis membrane (MWCO of 2 kDa) for 48 h and subsequently lyophilized. The amount of DOX loaded in the unimolecular micelles was measured by a UV-vis spectrophotometer at 485 nm.

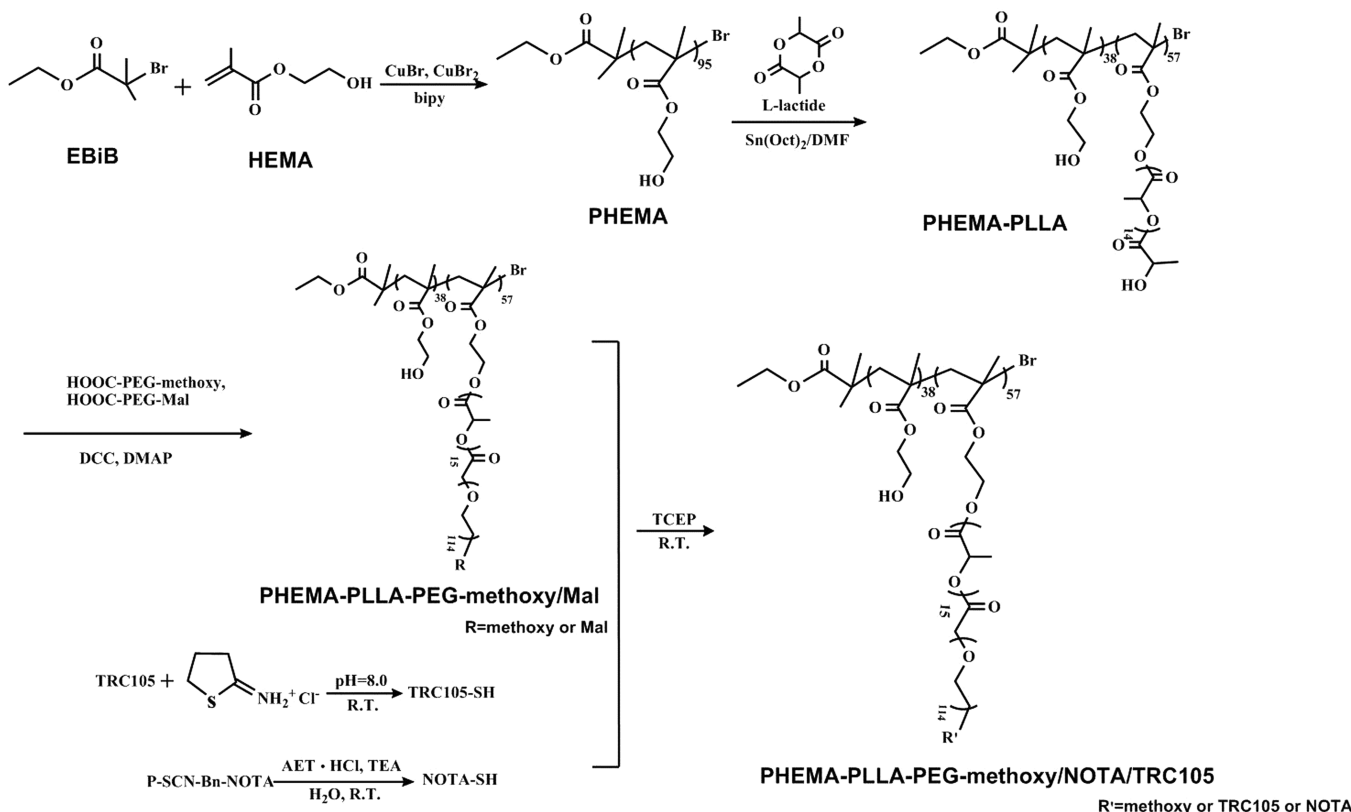
**In vitro Drug Release Study.** Drug release studies were conducted in acetate buffered solutions (ABS, pH 5.3) and phosphate buffered solutions (PBS, pH 7.4). Ten milligrams of DOX-loaded micelles were dispersed in 5 mL of media and placed in a dialysis bag (MWCO of 2 kDa). The dialysis bag was immersed in an apparatus containing 50 mL of a PBS or ABS buffer solution. The apparatuses were stored at 37 °C in a horizontal shaker (100 rpm). Released media (3 mL) were periodically removed and replaced by the same amount of fresh medium. The amount of released DOX was measured by a UV-vis spectrophotometer.

**Cell Uptake Study.** The cellular internalization and intracellular distribution of DOX-loaded micelles were studied with fluorescence microscopy and flow cytometry. For flow cytometry, CD105-positive<sup>28,34</sup> HUVECs were cultured into 6-well culture plates with M-200 overnight. After digestion with 0.05% trypsin, the cells ( $5 \times 10^6$  per mL) were treated with DOX-loaded micelles (both nontargeted and targeted) for 15 and 120 min at a DOX concentration of 20  $\mu$ g/mL. Micelle internalization was analyzed by detection of DOX fluorescence in a BD FACS Calibur four-color analysis cytometer (Becton Dickinson, San Jose, CA, USA). The resulting fluorescence histograms were processed using FlowJo software (v7.6, Tree Star, Inc., Ashland, OR, USA) with a minimum detection of  $1 \times 10^4$  cells and displayed on a four-decade log scale.

In our fluorescence microscopy studies, HUVEC or MCF-7 cells ( $1 \times 10^6$  per well) were cultured in 24-well cell culture plates with full media overnight. Cells were treated with DOX-loaded micelles (both targeted and nontargeted) for 120 min at a DOX concentration of 20  $\mu$ g/mL. An extra group of cells were incubated with DOX-loaded targeted micelles and 0.5 mg/mL of TRC105 (i.e., the blocking experiment) in order to confirm the CD105-specificity of these micelles at the cellular level. To maintain their appropriate morphology during treatment and observation, the HUVECs were fixed by a mixture of methanol/water/acetic acid (5:4:1) before micelle treatment. PBS was used to wash the unbound micelles from the cells after incubation. DOX fluorescence was recorded by a Nikon Eclipse Ti-U inverted microscope (Nikon, Melville, NY) with NIS-Elements BR Software.

**4T1 Murine Breast Cancer Model.** All animal studies were carried out following an animal protocol approved by the Institutional Animal Care and Use Committee at the University of Wisconsin. 4T1 murine breast cancer cells were used for tumor inoculation at ~80% confluence. Tumors were established by subcutaneous injection of  $2 \times 10^6$  cells (in 100  $\mu$ L of PBS) into the front flank of four- to five-

**Scheme 1. Synthetic Scheme for the Preparation of Brush-Shaped Amphiphilic PHEMA-PLLA-PEG-methoxy/TRC105/NOTA Block Copolymers**



week-old female Balb/c mice (Harlan, Indianapolis, IN). The mice were subjected to *in vivo* experiments when the tumors grew to 6 to 8 mm in diameter. We have detected previously high level CD105 expression in the neovasculature of 4T1 tumor tissue,<sup>28,29,35–38</sup> whereas the 4T1 cells were CD105-negative. Therefore, active tumor targeting was exclusively tumor vasculature-based in this study.

**<sup>64</sup>Cu-Labeling of Unimolecular Micelles.** Briefly, <sup>64</sup>CuCl<sub>2</sub> (111 MBq) was diluted in 300  $\mu$ L of sodium acetate buffer (0.1M, pH 6.5) and mixed with the micelle solution ( $\sim$ 2 mg/mL) at a 30  $\mu$ g (micelles) to 37 MBq (<sup>64</sup>CuCl<sub>2</sub>) ratio. The resulting mixture was reacted at 37 °C for 30 min under constant shaking. The <sup>64</sup>Cu-labeled targeted and nontargeted micelles were purified through PD-10 columns using PBS as the mobile phase before further studies.

**PET Imaging and Biodistribution Studies.** PET scans and image reconstruction (maximum a posteriori (MAP) algorithm, no attenuation or scatter correction) were performed using a microPET/microCT Inveon rodent model scanner (Siemens Medical Solutions USA, Inc.) at various time points postinjection (p.i.) as described previously.<sup>38–40</sup> After each scan, region-of-interest (ROI) analyses were conducted in each mouse with Inveon Research Workplace. <sup>64</sup>Cu-labeled targeted or nontargeted micelles were injected into each tumor-bearing mouse via the tail vein at a dose of 5 to 10 MBq per mouse before 3 to 15 min static PET scans were performed. Quantitative data were shown as percent injected dose per gram of tissue (%ID/g). For the competitive binding studies, one mg of competing TRC105 antibody was preinjected into four 4T1 tumor-bearing mice one hour before the <sup>64</sup>Cu-labeled targeted micelles was administered to the mice in order to further assess the CD105 specificity *in vivo*. Biodistribution studies (mean  $\pm$  SD) were conducted after the last PET scans using a gamma-counter (Perkin-Elmer) in order to validate the PET analysis.

## RESULTS

**Synthesis and Characterization of the Brush-Shaped Amphiphilic Block Copolymers.** The brush-shaped amphiphilic PHEMA-PLLA-PEG-methoxy/TRC105/NOTA block copolymer was synthesized following the steps shown in Scheme 1. PHEMA was synthesized by ATRP of HEMA with EBiB as an initiator and CuBr/2,2-bipyridine as the catalyst. The obtained functional polymeric backbone, defined as PHEMA, was analyzed by <sup>1</sup>H NMR using DMSO-d<sub>6</sub> as the solvent (Figure 2a). The peaks at about (a) 1.74 and (b) 0.76 ppm were attributed to the protons of the methine and methyl groups in the PHEMA main chains, respectively. The peaks at about (c) 3.88, (d) 3.58, and (e) 4.78 ppm were ascribed to the protons of the methylene groups and hydroxyl of PHEMA side chains. Based on GPC measurements, PHEMA had a number average molecular weight ( $M_n$ ) of 12,510 Da and a PDI ( $M_w/M_n$ ) of 1.379. The degree of polymerization of the PHEMA polymer was around (12510–195)/130 = 95.

The <sup>1</sup>H NMR spectrum of PHEMA-PLLA in DMSO-d<sub>6</sub> is shown in Figure 2b. The peaks at about (f) 5.17 and (h) 1.46 ppm were assigned to the protons of methine and methyl groups in the PLLA chains, respectively. The peak at (g) 4.18 ppm corresponded with the terminal methine protons of PLLA [HOCH(CH<sub>3</sub>)<sub>n</sub>] of PHEMA-PLLA. The peak at about (i) 1.27 ppm was due to the protons of the methyl groups of PLLA [HOCH(CH<sub>3</sub>)<sub>n</sub>]. The  $M_n$  and  $M_w/M_n$  of PHEMA-PLLA were about 73,662 Da and 1.328, respectively. The repeat units of the PLLA segment were 15 based on the intensity ratio of the peaks at (h) 1.46 ppm, which corresponded with the methyl groups in the PLLA polymer chain, to the peak at (i) 1.27 ppm, which corresponded with the methyl group adjacent to the

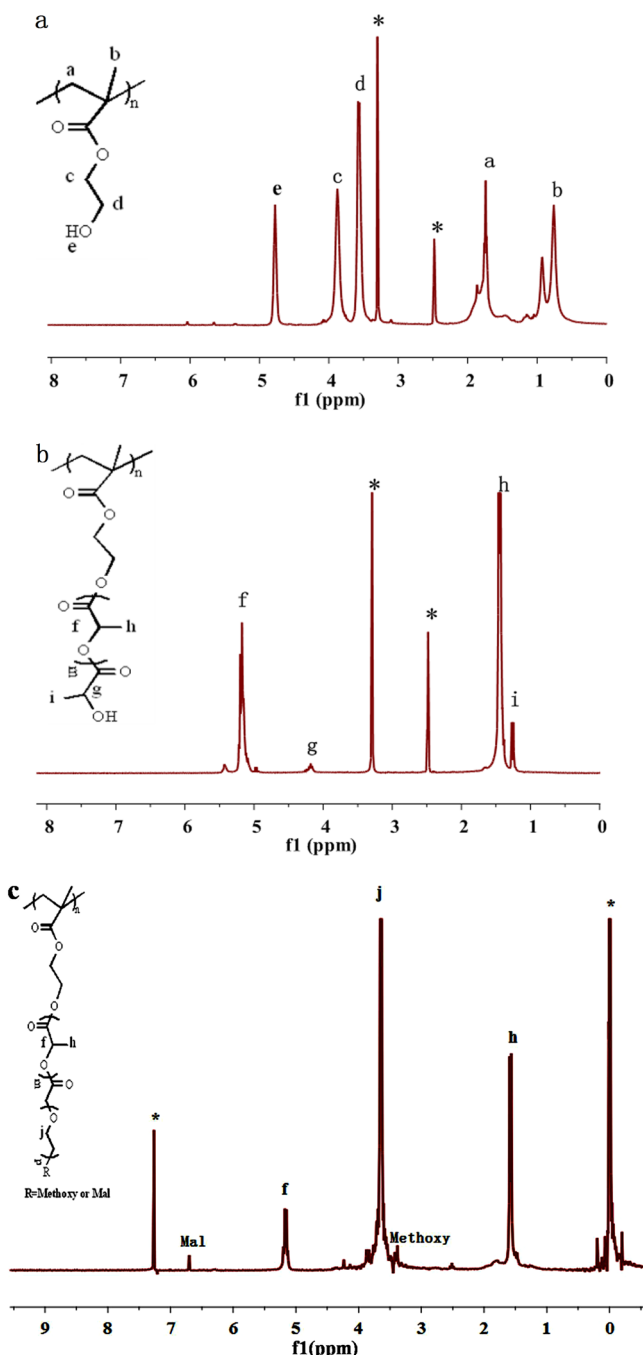


**Figure 2.** (a)  $^1\text{H}$  NMR spectrum of PHEMA. (b)  $^1\text{H}$  NMR spectrum of PHEMA-PLLA. (c)  $^1\text{H}$  NMR spectrum of PHEMA-PLLA-PEG.

hydroxyl end group.<sup>20</sup> The number of PLLA arms in PHEMA-PLLA was determined to be 57, based on the molecular weight difference between PHEMA and PHEMA-PLLA as determined by GPC using the equation

$$\begin{aligned} \text{no. of arms} &= (M_n(\text{PHEMA}) - M_n(\text{PLLA})) \\ &\quad / M_n(\text{PLLA}) \\ &= (73\,662 - 12\,510) / (72\cdot15) = 57 \end{aligned}$$

Brush-shaped amphiphilic PHEMA-PLLA-PEG-methoxy/Mal block copolymers were obtained via a reaction between the hydroxyl groups of PHEMA-PLLA and the carboxyl groups of PEG (HOOC-PEG-methoxy and HOOC-PEG-Mal), resulting

in ester linkages. In the  $^1\text{H}$  NMR spectrum of PHEMA-PLLA-PEG-methoxy/Mal (Figure 2c), the peaks at (j) 3.67 ppm and 3.40 ppm emerged because of the methylene protons of the oxyethylene units and the methoxyl protons of PEG-methoxy in addition to the peaks from the PLLA blocks. The peak at 6.68 ppm was attributed to the protons of the maleimide groups. According to the relative intensity ratio of the peaks at 6.68 ppm and (j) 3.67 ppm (which corresponded to the protons of the maleimide groups and the methylene protons in the PEG chains, respectively), the molar ratio of maleimide groups was 32%. The  $^1\text{H}$  NMR spectra clearly demonstrated the structure of the brush-shaped amphiphilic block copolymer PHEMA-PLLA-PEG-methoxy/Mal, which was further confirmed by GPC. Table 1 shows the molecular weights ( $M_n$ ) of

**Table 1.** Molecular Weights of PHEMA, PHEMA-PLLA, and PHEMA-PLLA-PEG-methoxy/Mal Measured by GPC

sample	$M_n$ (Da)	$M_w$ (Da)	$M_w/M_n$
PHEMA	12 510	17 251	1.379
PHEMA-PLLA	73 662	97 823	1.328
PHEMA-PLLA-PEG-methoxy/Mal	355 580	523 414	1.472

the PHEMA, PHEMA-PLLA, and PHEMA-PLLA-PEG-methoxy/Mal measured by GPC. The average number of the PLLA-PEG arms per PHEMA-PLLA-PEG-methoxy/Mal was calculated to be 56 according to the equation

$$\begin{aligned} \text{no. of arms} &= (M_n(\text{PHEMA}) - M_n(\text{PLLA}) - M_n(\text{PEG})) \\ &\quad / (M_n(\text{PEG})) \\ &= (355\,580 - 73\,662) / (5000) \\ &= 56 \end{aligned}$$

This is in good agreement with the number of PLLA arms for PHEMA-PLLA. TRC105 and NOTA were conjugated onto the surface of the PHEMA-PLLA-PEG-methoxy/Mal via interactions between maleimide and thiols on TRC105-SH (with  $\sim 5$  thiol groups per TRC105-SH<sup>28</sup>) and NOTA-SH. The PHEMA-PLLA-PEG-methoxy/NOTA, defined as nontargeted (without TRC105) micelles, was synthesized in a similar manner.

**Properties of Unimolecular Micelles Formed by Brush-Shaped Amphiphilic Block Copolymers.** The morphology of the unimolecular micelles were analyzed using TEM and DLS. Figure 3a shows the DLS data. The diameter of the micelles ranged from 55 to 150 nm. The average diameter was around 86 nm. The TEM images (Figure 3b) showed well-dispersed spherical nanoparticles with a typical size ranging from 22 to 30 nm. The sizes of the micelles measured by DLS were larger than those measured by TEM because TEM measures the sizes of the dried nanoparticles, whereas DLS measures the hydrodynamic diameters (sizes) of the nanoparticles that were dispersed in an aqueous solution, with the hydrophilic PEG segments of the amphiphilic PLLA-PEG arms extending freely into the aqueous solution.

**Drug Release Study.** The drug loading content in the DOX-loaded micelles was 16.7 wt %. The release profiles of the drug from the DOX-loaded micelles were evaluated at 37 °C under acidic (ABS, pH 5.3) and simulated physiological (PBS, pH 7.4) conditions. It was found that the DOX release profiles had a strong dependence on the pH values of the media (Figure

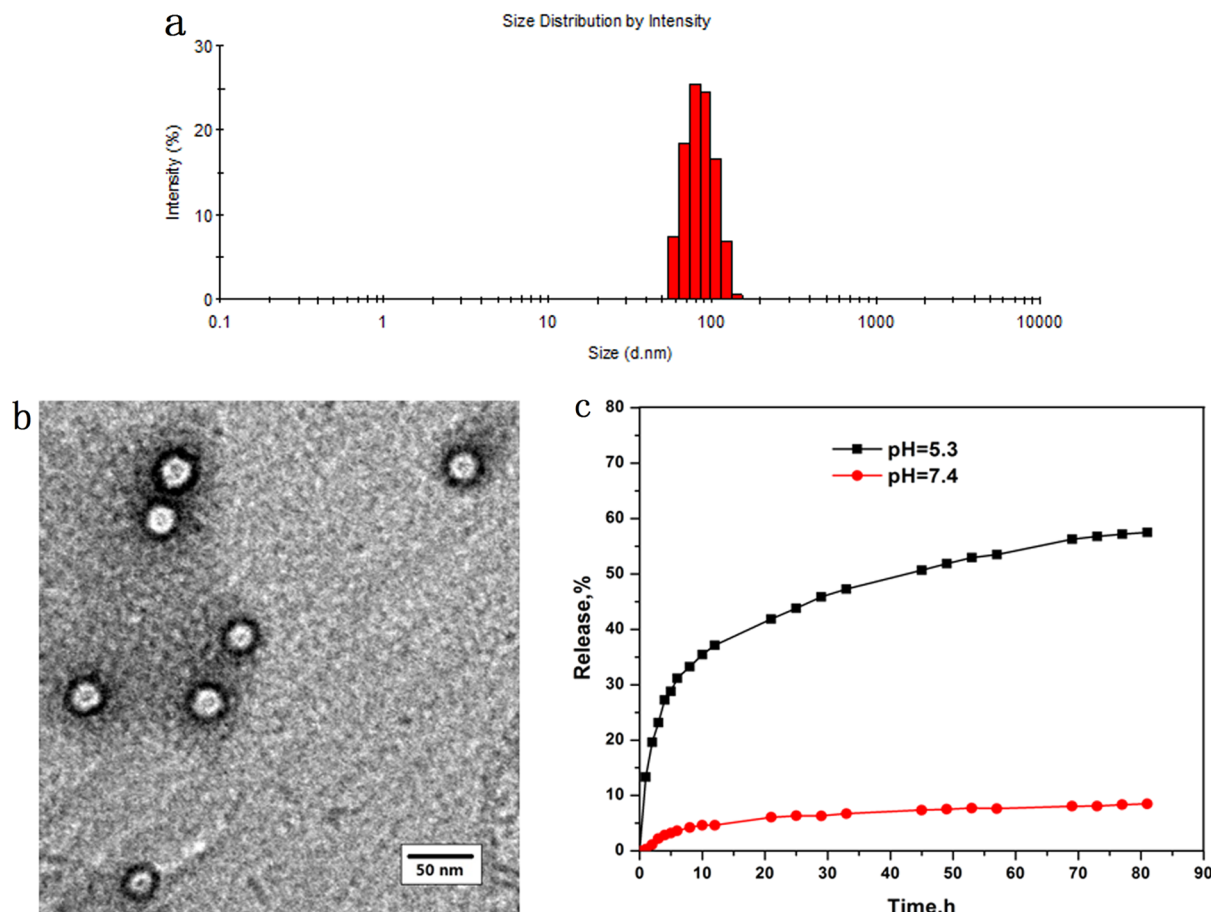


**Figure 3.** Characterization of unimolecular micelles. (a) A DLS histogram. (b) Representative TEM image. (c) In vitro drug release profiles of DOX-loaded unimolecular micelles at pH 7.4 (●) and pH 5.3 (■).

3c). At a pH of 5.3, about 32% of DOX was released after the first 6 h, and it rose to 60% in the following 76 h. In contrast, at a pH of 7.4, no apparent initial burst release was observed and only 9.0% of DOX was released after 82 h of incubation.

**CD105-Mediated Cellular Uptake.** In the fluorescent microscopy studies, a higher level of cellular DOX fluorescence was observed in HUVECs treated with targeted unimolecular micelles. In contrast, minimal cytoplasmic DOX fluorescence appeared in HUVECs treated with nontargeted micelles. Blocking with 0.5 mg/mL of TRC105 significantly reduced the cellular fluorescence of targeted micelles to a level comparable to that of nontargeted micelles (Figure 4a). Compared with HUVECs, a very low cellular uptake of both targeted and nontargeted micelles in MCF-7 (with no obvious difference) further confirmed that the cellular uptake of targeted micelles in HUVECs was CD105-mediated and specific.

Quantitative flow cytometry results in HUVEC for the cellular internalization of targeted micelles and nontargeted micelles at an early (15 min) and late (120 min) time point are shown in Figure 4b. Cells with no addition of either micelle were adopted as a negative control, in which only negligible levels of autofluorescence were documented at both time points. As early as 15 min post-treatment, the cellular uptake of targeted micelles in HUVEC was >50% higher than that of nontargeted micelles. At 120 min, the cellular uptake of DOX revealed a pronounced increase for all treatment groups. Again, a significantly higher level of cellular fluorescence was observed

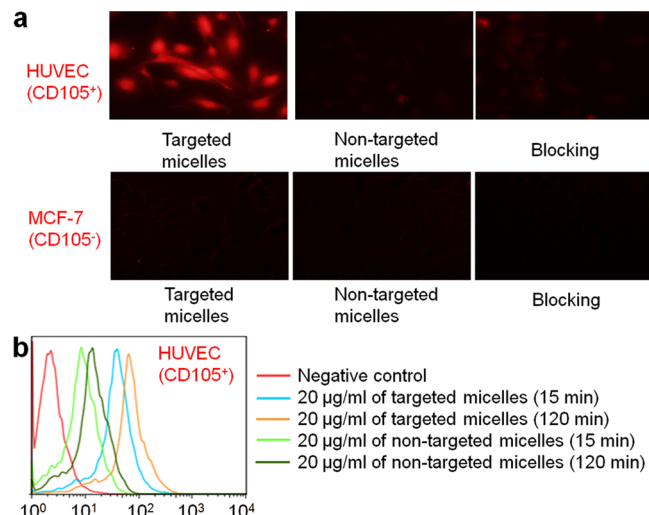


**Figure 4.** (a) Fluorescence microscopy images of HUVEC and MCF-7 cells incubated with targeted micelles, nontargeted micelles, or targeted micelles with a blocking dose of TRC105 at 37 °C for 2 h. All samples had a DOX concentration of 20 µg/mL. (b) Flow cytometry analysis of HUVECs treated with targeted or nontargeted micelles (all with equivalent DOX concentrations of 20 µg/mL) for 15 and 120 min at 37 °C.

in cells treated with targeted micelles compared to cells treated with nontargeted micelles. Combining these facts, the cell-based assays confirmed that TRC105 conjugation contributed

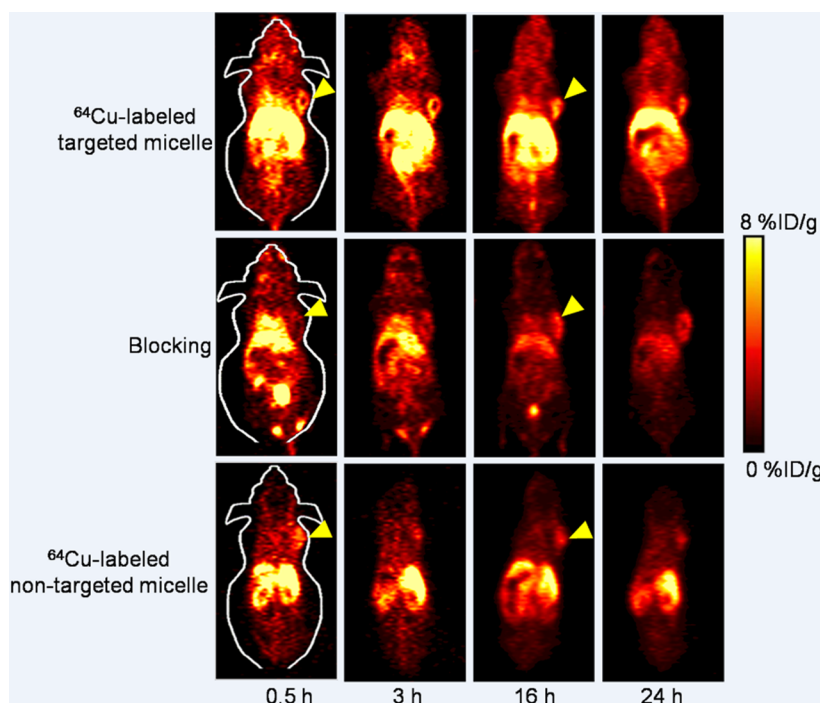


**Figure 5.** Serial coronal PET images of 4T1 tumor-bearing mice at different time points postinjection of  $^{64}\text{Cu}$ -labeled targeted, nontargeted micelles, or targeted micelles with a blocking dose of TRC105. Images are representative of 3 mice per group.

to the enhanced cellular uptake of PHEMA-based unimolecular micelles, and more specifically, via binding to CD105 and subsequent internalization.

**$^{64}\text{Cu}$ -Labeling and PET Imaging.** The whole reaction time for  $^{64}\text{Cu}$ -labeling and purification was  $70 \pm 10$  min ( $n = 6$ ). The decay-corrected radiochemical yield of  $57.5 \pm 14.3\%$  was achieved in this study based on  $30 \mu\text{g}$  of unimolecular micelles (targeted or nontargeted) per 37 MBq of  $^{64}\text{Cu}$ , with a radiochemical purity of  $>95\%$ . The ratio of  $^{64}\text{Cu}$  activity to micelles was counted to be  $\sim 0.6$  GBq/mg of micelles, assuming no loss of unimolecular micelles after purification.

Short-term and long-term behavior of the targeted and nontargeted unimolecular micelles were both investigated in this study at time points of 0.5, 3, 16, and 24 h p.i., all of which were chosen for PET scans based on our previous experience.<sup>7,8,28,36</sup> The 4T1 tumor-containing coronal PET slices are shown in Figure 5. From the noticeably different radioactivity level in the blood pool, we concluded that the circulation half-life of  $^{64}\text{Cu}$ -labeled targeted micelles was significantly longer than that of  $^{64}\text{Cu}$ -labeled nontargeted micelles (a few hours vs  $<0.5$  h), which can facilitate in vivo tumor targeting. The primary accumulation tissues/organs of  $^{64}\text{Cu}$ -labeled targeted micelles included the liver, tumor, spleen, kidneys, and intestines. On the other hand, the uptake of  $^{64}\text{Cu}$ -labeled targeted micelles in most normal tissues (e.g., muscle, bone, brain, etc.) was very low, conferring high tumor-targeting efficacy and good image contrast. Overall, the tumor accumulation of  $^{64}\text{Cu}$ -labeled nontargeted micelles, as well as  $^{64}\text{Cu}$ -labeled targeted micelles with TRC105 blocking, was at a low background level (Figure 5), which can be numerically illustrated by ROI analysis as discussed below.

Quantitative ROI analyses of the PET images are shown in Figure 6. Similar to most intravenously injected nanomaterials, a prominent liver uptake of  $^{64}\text{Cu}$ -labeled targeted micelles at early time points with a gradual decline ( $22.2 \pm 0.8$ ,  $17.8 \pm 0.4$ ,

$14.0 \pm 0.5$ , and  $11.4 \pm 1.4\%$  ID/g at 0.5, 3, 16, and 24 h p.i., respectively;  $n = 3$ ) was detected. Radioactivity of  $^{64}\text{Cu}$ -labeled targeted micelles in the blood was  $9.7 \pm 0.4$ ,  $7.5 \pm 0.2$ ,  $5.4 \pm 0.2$ , and  $4.8 \pm 0.4\%$  ID/g at 0.5, 3, 16, and 24 h p.i., respectively ( $n = 3$ ; Figure 6a). The 4T1 tumor uptake of  $^{64}\text{Cu}$ -labeled targeted micelles was readily detectable at 0.5 h p.i., peaked at 3 h p.i., and plateaued after 3 h p.i. ( $5.7 \pm 0.5$ ,  $5.9 \pm 0.7$ ,  $4.7 \pm 0.7$ , and  $3.8 \pm 0.6\%$  ID/g at 0.5, 3, 16, and 24 h p.i., respectively;  $n = 3$ , Figure 6a). A tumor/muscle ratio of  $9.1 \pm 2.3$  was achieved for  $^{64}\text{Cu}$ -labeled targeted micelles at 3 h p.i. ( $n = 3$ ), confirming satisfactory tumor contrast.

A blocking dose of TRC105 (1 mg per mouse) reduced the 4T1 tumor uptake of  $^{64}\text{Cu}$ -labeled targeted micelles significantly ( $2.0 \pm 0.3$ ,  $2.2 \pm 0.5$ ,  $2.7 \pm 0.7$ , and  $2.6 \pm 0.3\%$  ID/g at 0.5, 3, 16, and 24 h p.i., respectively;  $n = 3$ ; see Figure 6b, which served as strong evidence for the CD105 specificity of  $^{64}\text{Cu}$ -labeled targeted micelles in vivo. Liver uptake from the blocking group was similar to that of  $^{64}\text{Cu}$ -labeled targeted micelles at early time points, but a sharper decrease was noticeable after 3 h p.i. ( $16.5 \pm 2.7$ ,  $10.4 \pm 1.9$ ,  $6.3 \pm 0.5$ , and  $4.3 \pm 0.4\%$  ID/g at 0.5, 3, 16, and 24 h p.i., respectively;  $n = 3$ ; Figure 6b).

The use of  $^{64}\text{Cu}$ -labeled nontargeted micelles in the PET study was to investigate the tumor uptake from passive targeting alone. The tumor uptake of  $^{64}\text{Cu}$ -labeled nontargeted micelles ( $4.0 \pm 0.6$ ,  $3.2 \pm 0.7$ ,  $2.2 \pm 0.2$ , and  $2.0 \pm 0.1\%$  ID/g at 0.5, 3, 16, and 24 h p.i., respectively;  $n = 3$ ; Figure 6b, d) was significantly lower than that of  $^{64}\text{Cu}$ -labeled targeted micelles at all time points examined ( $p < 0.05$ ;  $n = 3$ ). The blood-pool radioactivity of  $^{64}\text{Cu}$ -labeled nontargeted micelles was also significantly lower when compared with that of  $^{64}\text{Cu}$ -labeled targeted micelles ( $3.0 \pm 1.0$ ,  $2.8 \pm 0.6$ ,  $2.4 \pm 0.3$ , and  $2.3 \pm 0.2\%$  ID/g at 0.5, 3, 16, and 24 h p.i., respectively;  $n = 3$ ; Figure 6c).

Biodistribution studies were conducted at 24 h p.i. in all major organs/tissues to further validate the in vivo PET data

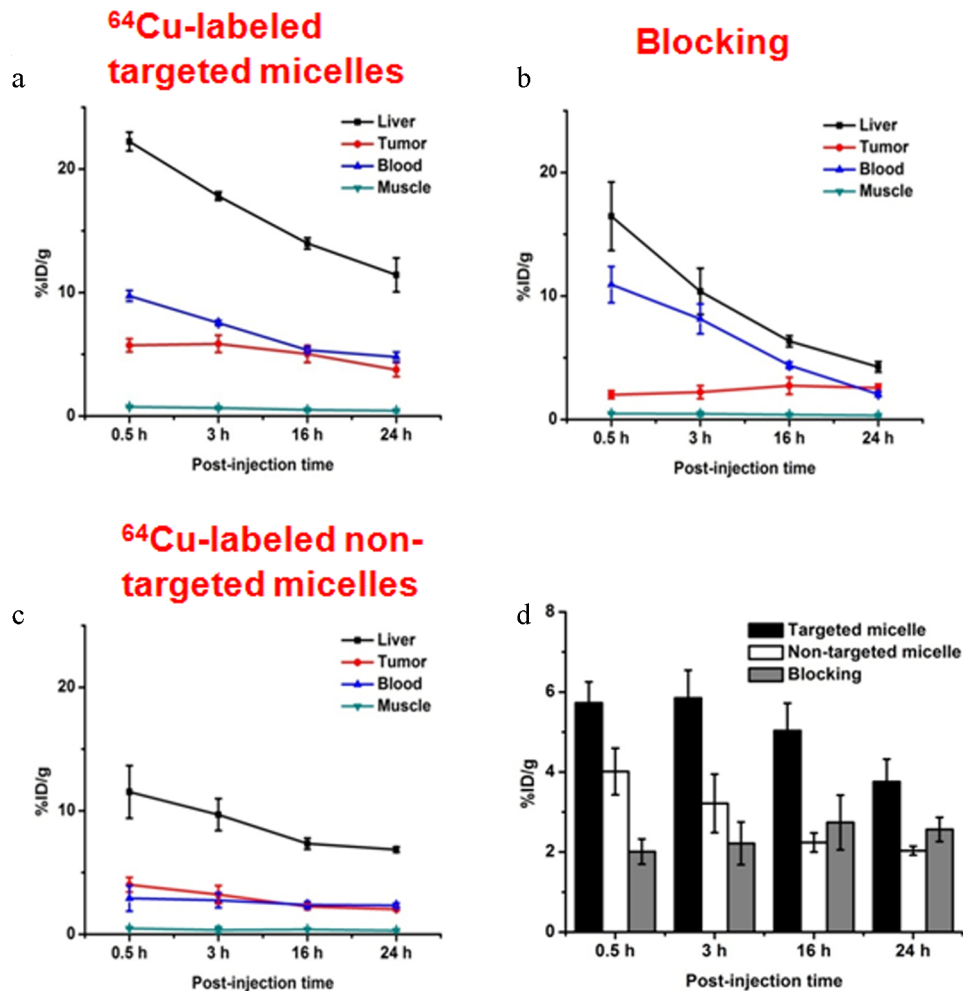


**Figure 6.** Region-of-interest analysis of PET data. (a) Time-activity curves of the liver, 4T1 tumor, blood, and muscle upon intravenous injection of  $^{64}\text{Cu}$ -labeled targeted micelles ( $n = 3$ ). (b) Time-activity curves of the liver, 4T1 tumor, blood, and muscle upon intravenous injection of  $^{64}\text{Cu}$ -labeled targeted micelles after preinjection of a blocking dose of TRC105 ( $n = 3$ ). (c) Time-activity curves of the liver, 4T1 tumor, blood, and muscle upon intravenous injection of  $^{64}\text{Cu}$ -labeled nontargeted micelles ( $n = 3$ ). (d) Comparison of 4T1 tumor uptake for  $^{64}\text{Cu}$ -labeled targeted, nontargeted micelles, and targeted micelles with TRC105 blocking at different time points postinjection.

(Figure 7). The biodistribution pattern of  $^{64}\text{Cu}$ -labeled targeted micelles at tumor uptake peak time (3 h p.i. based on PET) was also evaluated in a separate group of three mice. Prominent uptake of  $^{64}\text{Cu}$ -labeled targeted micelles in the 4T1 tumor was observed in this subgroup, which was only lower than the organs responsible for clearance. Overall, the quantification results obtained from the biodistribution studies and PET scans were highly consistent, confirming that the quantitative ROI analysis of PET reflected the real-time distribution patterns of  $^{64}\text{Cu}$ -labeled micelles *in vivo*.

## DISCUSSION

Targeted drug delivery and controlled drug release offered by nanomedicine can significantly enhance the therapeutic outcome of cancer therapy while sparing the normal tissues/ organs. In recent years, significant effort has been devoted to preparing unimolecular micelles from dendrimers, hyperbranched polymers, etc.<sup>7,17,18,31,41</sup> In contrast to multimolecular micelle self-assembled from a large number of linear amphiphilic block copolymer molecules, unimolecular micelle formed by single dendritic amphiphilic block copolymer molecule exhibits excellent *in vivo* stability due to their covalent nature. In addition, unimolecular micelles possess the

following two characteristics to make them highly desirable as drug nanocarriers: first, their structures can be readily controlled by tailoring the type and functionality of the core, and the molecular weight and chemical composition of the amphiphilic block copolymer arms; second, synthesis can be quite simple when compared to the tedious step-by-step synthesis required for certain well-defined dendrimers.<sup>42</sup>

Poly(2-hydroxyethyl methacrylate), PHEMA, is an important polymer for biomedical applications. Its excellent biocompatibility makes PHEMA readily applicable for artificial blood plasma or soft contact lenses.<sup>43</sup> At the same time, PHEMA has a side terminal hydroxyl group in each unit that provides attachment sites for other polymer segments, targeting moieties, or drug molecules. In this study, PHEMA was used as the macroinitiator for the ROP of the hydrophobic segment (i.e., PLLA) of the amphiphilic PLLA-PEG arms utilizing these side hydroxyl groups (Figure 1 and Scheme 1). Although certain PHEMA copolymers were investigated as potential anticancer drug carriers,<sup>44</sup> the use of brush-shaped amphiphilic PHEMA-PLLA-PEG block copolymers combined with active targeting ligands as drug carriers has not been reported to date to the best of our knowledge. PHEMA was synthesized by ATRP, one of the most widely used controlled radical

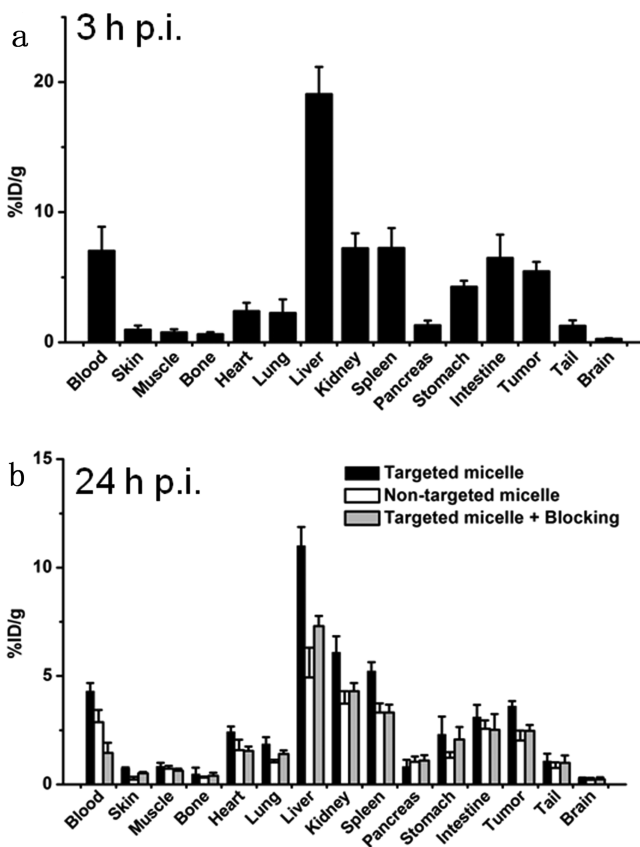


**Figure 7.** (a) Biodistribution of  $^{64}\text{Cu}$ -labeled targeted micelles at 3 h postinjection. (b) Biodistribution of  $^{64}\text{Cu}$ -labeled targeted micelles, nontargeted micelles, and targeted micelles with TRC105 blocking at 24 h postinjection.  $n = 3$  per group.

polymerization techniques for the preparation of well-defined polymeric structures with controlled molecular weights and narrow PDI.<sup>45</sup> Although it was predicted that brush-shaped amphiphilic block copolymers could form worm-like unimolecular micelles, spherical micelles were found in the TEM images (Figure 3b). While the exact reasons are unknown at this time, many factors such as the chemical structure of the dendritic copolymer, side chain interactions, and the solvent effect may all play a role in determining the final shape of the nanoparticles.<sup>46,47</sup>

The drug release profile of the drug-loaded unimolecular micelles exhibited strong pH sensitivity likely due to protonation of the amino group present in DOX, as well as faster degradation of the hydrophobic core of the micelles under acidic conditions (Figure 3c). This pH-sensitive drug release behavior is favorable for targeted cancer therapy. Specifically, the amount of DOX released prematurely during circulation can be minimized; meanwhile, DOX can be released relatively quickly in the acidic endosomal/lysosomal compartments once the DOX-loaded micelles are taken up by the targeted cancer cells via CD105-mediated endocytosis, which can significantly improve the therapeutic outcome of cancer therapy while minimizing any undesirable side effects from DOX.<sup>48,49</sup>

CD105 is a well-accepted protein marker involved in tumor angiogenesis, with broad applicability to serve as a theranostic target for various solid tumors based on literature reports.<sup>25,26,50</sup> When compared to other molecular markers for tumor targeting and imaging, CD105 exhibited several potential

advantages such as abundant and universal expression in different tumor types (largely independent of CD105 expression level on cancer cells), direct accessibility from the bloodstream, and high specificity and selectivity from tumor-associated neovascularization. The conjugation of CD105-targeting antibodies (TRC105) onto unimolecular micelles significantly enhanced their uptake into CD105-positive cells *in vitro* (Figure 4), as well as their tumor targeting efficiency *in vivo* (Figures 5&6). These were successfully evaluated noninvasively with PET, a widely used clinical imaging technique in oncology,<sup>51,52</sup> which is quantitative, sensitive, and clinically translatable.<sup>53–55</sup> 4T1 was selected as the preferred tumor model in this study because of its fast-growing nature. It has a significant amount of tumor angiogenesis and hence high CD105 expression levels during the exponential growth stage, despite the fact that the 4T1 cells themselves are inherently CD105-negative.

One potential future research direction would be to optimize the targeting ligands on the micelles. Despite its high affinity to CD105, TRC105 can still have nonspecific interactions with Fc receptors *in vivo* from various types of cells (especially immune cells including but not limited to macrophages, neutrophils, dendritic cells, natural killer cells, and B cells).<sup>56</sup> To minimize these interactions, as well as any potential immune responses, we could use antibody fragments (Fab, F(ab')<sub>2</sub>, diabody, etc.) or peptides for future generations of unimolecular micelles.

## CONCLUSIONS

Multifunctional unimolecular micelles based on a novel brush-shaped amphiphilic block copolymer were developed for both tumor-targeted drug delivery and noninvasive PET imaging. Doxorubicin encapsulated within the unimolecular micelles was released over a sustained time period in a pH-dependent manner. The cellular uptake of TRC105-conjugated targeted unimolecular micelles (PHEMA-PLLA-PEG-TRC105) was proved to be much higher in CD105-positive cells than that of nontargeted micelles. A much higher level of tumor accumulation was also demonstrated in 4T1 murine breast tumor-bearing mice treated with  $^{64}\text{Cu}$ -labeled targeted micelles when compared with those treated with nontargeted ones based on the PET imaging and ex vivo biodistribution studies. These multifunctional tumor-targeting unimolecular micelles with pH-controllable drug release profiles, and PET imaging capability are promising drug/agent nanocarriers for targeted cancer theranostics.

## AUTHOR INFORMATION

### Corresponding Authors

\*E-mail: wcai@uwhealth.org.  
\*E-mail: sgong@engr.wisc.edu.

### Author Contributions

<sup>†</sup>Authors J.G. and H.H. contributed equally.

### Notes

The authors declare no competing financial interest.

## ACKNOWLEDGMENTS

We acknowledge the financial support from the National Institutes of Health (1K25CA166178, NIBIB/NCI 1R01CA169365-01A1), National Science Foundation (DMR 1032187), the Scientific Research Foundation for Returned Overseas Chinese Scholars, State Education Ministry, P. R. China, the Department of Defense (W81XWH-11-1-0644),

and the American Cancer Society (125246-RSG-13-099-01-CCE).

## ■ REFERENCES

- (1) Hainfeld, J. F.; Smilowitz, H. M.; O'Connor, M. J.; Avraham, F. Dilmanian; Slatkin, D. N. Gold Nanoparticle Imaging and Radiotherapy of Brain Tumors in Mice. *Nanomedicine* **2013**, *8*, 1601.
- (2) Wang, L. S.; Chuang, M. C.; Ho, J. A. Nano-theranostics—a Review of Recent Publications. *Int. J. Nanomed.* **2012**, *7*, 4679.
- (3) Feng, X. L.; Lv, F. T.; Liu, L. B.; Tang, H. W.; Xing, C. F.; Yang, Q.; Wang, S. Conjugated Polymer Nanoparticles for Drug Delivery and Imaging. *ACS Appl. Mater. Interfaces* **2010**, *2*, 2429–2435.
- (4) Deng, D. W.; Qu, L. Z.; Zhang, J.; Ma, Y. X.; Gu, Y. Q. Quaternary Zn–Ag–In–Se Quantum Dots for Biomedical Optical Imaging of RGD-Modified Micelles. *ACS Appl. Mater. Interfaces* **2013**, *5*, 10858–10865.
- (5) Chen, X. S. One Year after a Successful Start of Theranostics. *Theranostics* **2012**, *2*, 1.
- (6) Yang, F.; Wang, Q.; Gu, Z. X.; Fang, K.; Marriott, G.; Gu, N. Silver Nanoparticle-Embedded Microbubble as a Dual-Mode Ultrasound and Optical Imaging Probe. *ACS Appl. Mater. Interfaces* **2013**, *5*, 9217–9223.
- (7) Xiao, Y.; Hong, H.; Javadi, A.; Engle, J. W.; Xu, W.; Yang, Y.; Zhang, Y.; Barnhart, T. E.; Cai, W.; Gong, S. Multifunctional Unimolecular Micelles for Cancer-Targeted Drug Delivery and Positron Emission Tomography Imaging. *Biomaterials* **2012**, *33*, 3071.
- (8) Yang, X.; Hong, H.; Grailer, J. J.; Rowland, I. J.; Javadi, A.; Hurley, S. A.; Xiao, Y.; Yang, Y.; Zhang, Y.; Nickles, R. J.; Cai, W.; Steeber, D. A.; Gong, S. cRGD-Functionalized, DOX-Conjugated, and <sup>64</sup>Cu-Labeled Superparamagnetic Iron Oxide Nanoparticles for Targeted Anticancer Drug Delivery and PET/MR Imaging. *Biomaterials* **2011**, *32*, 4151.
- (9) Gong, J.; Chen, M.; Zheng, Y.; Wang, S.; Wang, Y. Polymeric Micelles Drug Delivery System in Oncology. *J. Controlled Release* **2012**, *159*, 312.
- (10) Fu, Y. Z.; Su, Y. S.; Manthiram, A. Sulfur–Carbon Nanocomposite Cathodes Improved by an Amphiphilic Block Copolymer for High-Rate Lithium–Sulfur Batteries. *ACS Appl. Mater. Interfaces* **2012**, *4*, 6046–6052.
- (11) Kim, S.; Shi, Y.; Kim, J. Y.; Park, K.; Cheng, J. X. Overcoming the Barriers in Micellar Drug Delivery: Loading Efficiency, in Vivo Stability, and Micelle-Cell Interaction. *Expert Opin. Drug Deliv.* **2010**, *7*, 49.
- (12) Xu, W.; Burke, J. F.; Pilla, S.; Chen, H.; Jaskula-Sztul, R.; Gong, S. Octreotide-Functionalized and Resveratrol-Loaded Unimolecular Micelles for Targeted Neuroendocrine Cancer Therapy. *Nanoscale* **2013**, *5*, 9924.
- (13) Luo, S.; Ling, C.; Hu, X.; Liu, X.; Chen, S.; Han, M.; Xia, J. Thermoresponsive Unimolecular Micelles with a Hydrophobic Dendritic Core and a Double Hydrophilic Block Copolymer Shell. *J. Colloid Interface Sci.* **2011**, *353*, 76.
- (14) Kreutzer, G.; Ternat, C.; Nguyen, T. Q.; Plummer, C. J. G.; Månsen, J.-A. E.; Castelletto, V.; Hamley, I. W.; Sun, F.; Sheiko, S. S.; Herrmann, A.; Ouali, L.; Sommer, H.; Fieber, W.; Velazco, M. I.; Klok, H.-A. Water-Soluble, Unimolecular Containers Based on Amphiphilic Multiarm Star Block Copolymers. *Macromolecules* **2006**, *39*, 4507.
- (15) Geng, Y.; Dalhaimer, P.; Cai, S.; Tsai, R.; Tewari, M.; Minko, T.; Discher, D. E. Shape Effects of Filaments Versus Spherical Particles in Flow and Drug Delivery. *Nat. Nanotechnol.* **2007**, *2*, 249.
- (16) Cai, S.; Vijayan, K.; Cheng, D.; Lima, E. M.; Discher, D. E. Micelles of Different Morphologies—Advantages of Worm-Like Filomicelles of PEO-PCL in Paclitaxel Delivery. *Pharm. Res.* **2007**, *24*, 2099.
- (17) Prabaharan, M.; Grailer, J. J.; Pilla, S.; Steeber, D. A.; Gong, S. Folate-Conjugated Amphiphilic Hyperbranched Block Copolymers based on Boltorn® H40, Poly(L-lactide) and Poly(ethylene glycol) for Tumor-Targeted drug Delivery. *Biomaterials* **2009**, *30*, 3009.
- (18) Aryal, S.; Prabaharan, M.; Pilla, S.; Gong, S. Biodegradable and Biocompatible Multi-Arm Star Amphiphilic Block Copolymer as a Carrier for Hydrophobic Drug Delivery. *Int. J. Biol. Macromol.* **2009**, *44*, 346.
- (19) Zhi-Mei, M.; Si-Xue, C.; Xian-Zheng, Z.; Qing-Rong, W.; Zhuo, R.-X. Degradation and Drug Release Property of Star Poly(e-caprolactone)s with Dendritic Cores. *J. Biomed. Mater. Res. B: Appl. Biomater.* **2006**, *81B*, 40.
- (20) Prabaharan, M.; Grailer, J. J.; Pilla, S.; Steeber, D. A.; Gong, S. Amphiphilic Multi-Arm Block Copolymer based on Hyperbranched Polyester, Poly(L-lactide) and Poly(ethylene glycol) as a Drug Delivery Carrier. *Macromol. Biosci.* **2009**, *9*, 515.
- (21) Zhu, S.; Hong, M.; Zhang, L.; Tang, G.; Jiang, Y.; Pei, Y. PEGylated PAMAM Dendrimer-Doxorubicin Conjugates: in Vitro Evaluation and in Vivo Tumor Accumulation. *Pharm. Res.* **2010**, *27*, 161.
- (22) Si, C.; Xian-Zheng, Z.; Si-Xue, C.; Ren-Xi, Z.; Gu, Z.-W. Functionalized Amphiphilic Hyperbranched Polymers for Targeted Drug Delivery. *Biomacromolecules* **2008**, *9*, 2578.
- (23) Zhao, P.; Liu, L.; Feng, X.; Wang, C.; Shuai, X.; Chen, Y. Molecular Nanoworm with PCL Core and PEO Shell as a Non-Spherical Carrier for Drug Delivery. *Macromol. Rapid Commun.* **2012**, *33*, 1351.
- (24) Yan, Geng; Discher, D. E. Hydrolytic Degradation of Poly(ethylene oxide)-block-polycaprolactone Worm Micelles. *J. Am. Chem. Soc.* **2005**, *127*, 12780.
- (25) Dallas, N. A.; Samuel, S.; Xia, L.; Fan, F.; Gray, M. J.; Lim, S. J.; Ellis, L. M. Endoglin (CD105): A Marker of Tumor Vasculature and Potential Target for Therapy. *Clin. Cancer Res.* **2008**, *14*, 1931.
- (26) Seon, B. K.; Haba, A.; Matsuno, F.; Takahashi, N.; Tsujie, M.; She, X.; Harada, N.; Uneda, S.; Tsujie, T.; Toi, H.; Tsai, H.; Haruta, Y. Endoglin-Targeted Cancer Therapy. *Curr. Drug Delivery* **2011**, *8*, 135.
- (27) Engle, J. W.; Hong, H.; Zhang, Y.; Valdovinos, H. F.; Myklejord, D. V.; Barnhart, T. E.; Theuer, C. P.; Nickles, R. J.; Cai, W. Positron Emission Tomography Imaging of Tumor Angiogenesis with a <sup>66</sup>Ga-Labeled Monoclonal Antibody. *Mol. Pharm.* **2012**, *9*, 1441.
- (28) Hong, H.; Yang, K.; Zhang, Y.; Engle, J. W.; Feng, L.; Yang, Y.; Nayak, T. R.; Goel, S.; Bean, J.; Theuer, C. P.; Barnhart, T. E.; Liu, Z.; Cai, W. In Vivo Targeting and Imaging of Tumor Vasculature with Radiolabeled, Antibody-Conjugated Nanographene. *ACS Nano* **2012**, *6*, 2361.
- (29) Hong, H.; Zhang, Y.; Engle, J. W.; Nayak, T. R.; Theuer, C. P.; Nickles, R. J.; Barnhart, T. E.; Cai, W. In Vivo Targeting and Positron Emission Tomography Imaging of Tumor Vasculature with <sup>66</sup>Ga-Labeled Nano-Graphene. *Biomaterials* **2012**, *33*, 4147.
- (30) Zhang, Y.; Hong, H.; Engle, J. W.; Bean, J.; Yang, Y.; Leigh, B. R.; Barnhart, T. E.; Cai, W. Positron Emission Tomography Imaging of CD105 Expression with a <sup>64</sup>Cu-Labeled Monoclonal Antibody: NOTA is Superior to DOTA. *PLoS One* **2011**, *6*, e28005.
- (31) Guo, J.; Hong, H.; Chen, G.; Shi, S.; Zheng, Q.; Zhang, Y.; Theuer, C. P.; Barnhart, T. E.; Cai, W.; Gong, S. Image-Guided and Tumor-Targeted Drug Delivery with Radiolabeled Unimolecular Micelles. *Biomaterials* **2013**, *34*, 8323.
- (32) Hong, H.; Zhang, Y.; Severin, G. W.; Yang, Y.; Engle, J. W.; Niu, G.; Nickles, R. J.; Chen, X.; Leigh, B. R.; Barnhart, T. E.; Cai, W. Multimodality Imaging of Breast Cancer Experimental Lung Metastasis with Bioluminescence and a Monoclonal Antibody Dual-Labeled with <sup>(89)Zr</sup> and IRDye 800CW. *Mol. Pharm.* **2012**, *9*, 2339.
- (33) Rosen, L. S.; Hurwitz, H. I.; Wong, M. K.; Goldman, J.; Mendelson, D. S.; Figg, W. D.; Spencer, S.; Adams, B. J.; Alvarez, D.; Seon, B. K.; Theuer, C. P.; Leigh, B. R.; Gordon, M. S. A Phase I First-in-Human Study of TRC105 (Anti-Endoglin Antibody) in Patients with Advanced Cancer. *Clin. Cancer Res.* **2012**, *18*, 4820.
- (34) Hong, H.; Yang, Y.; Zhang, Y.; Engle, J. W.; Barnhart, T. E.; Nickles, R. J.; Leigh, B. R.; Cai, W. Positron Emission Tomography Imaging of CD105 Expression during Tumor Angiogenesis. *Eur. J. Nucl. Med. Mol. Imaging* **2011**, *38*, 1335.
- (35) Hong, H.; Severin, G. W.; Yang, Y.; Engle, J. W.; Zhang, Y.; Barnhart, T. E.; Liu, G.; Leigh, B. R.; Nickles, R. J.; Cai, W. Positron

- Emission Tomography Imaging of CD105 Expression with  $^{89}\text{Zr}$ -Df-TRC105. *Eur. J. Nucl. Med. Mol. Imaging* **2012**, *39*, 138.
- (36) Shi, S.; Yang, K.; Hong, H.; Valdovinos, H. F.; Nayak, T. R.; Zhang, Y.; Theuer, C. P.; Barnhart, T. E.; Liu, Z.; Cai, W. Tumor Vasculature Targeting and Imaging in Living Mice with Reduced Graphene Oxide. *Biomaterials* **2013**, *34*, 3002.
- (37) Zhang, Y.; Hong, H.; Engle, J. W.; Yang, Y.; Theuer, C. P.; Barnhart, T. E.; Cai, W. Positron Emission Tomography and Optical Imaging of Tumor CD105 Expression with a Dual-Labeled Monoclonal Antibody. *Mol. Pharm.* **2012**, *9*, 645.
- (38) Zhang, Y.; Hong, H.; Severin, G. W.; Engle, J. W.; Yang, Y.; Goel, S.; Nathanson, A. J.; Liu, G.; Nickles, R. J.; Leigh, B. R.; Barnhart, T. E.; Cai, W. ImmunoPET and Near-Infrared Fluorescence Imaging of CD105 Expression using a Monoclonal Antibody Dual-Labeled with  $(^{89}\text{Zr})$  and IRDye 800CW. *Am. J. Transl. Res.* **2012**, *4*, 333.
- (39) Zhang, Y.; Hong, H.; Engle, J. W.; Yang, Y.; Barnhart, T. E.; Cai, W. Positron Emission Tomography and Near-Infrared Fluorescence Imaging of Vascular Endothelial Growth Factor with Dual-Labeled Bevacizumab. *Eur. J. Nucl. Med. Mol. Imaging* **2012**, *2*, 1.
- (40) Hong, H.; Zhang, Y.; Severin, G. W.; Yang, Y.; Engle, J. W.; Niu, G.; Nickles, R. J.; Chen, X.; Leigh, B. R.; Barnhart, T. E.; Cai, W. Multimodality Imaging of Breast Cancer Experimental Lung Metastasis with Bioluminescence and a Monoclonal Antibody Dual-Labeled with  $(^{89}\text{Zr})$  and IRDye 800CW. *Mol. Pharm.* **2012**, *9*, 2339.
- (41) Wang, Y.; Grayson, S. M. Approaches for the Preparation of Non-Linear Amphiphilic Polymers and Their Applications to Drug Delivery. *Adv. Drug Delivery Rev.* **2012**, *64*, 852.
- (42) Li, J.; Li, J.; Xu, S.; Zhang, D.; Liu, D. Hydrophobic Oligopeptide-based Star-Block Copolymers as Unimolecular Nanocarriers for Poorly Water-Soluble Drugs. *Colloids Surf., B* **2013**, *110*, 183.
- (43) Nogueira, N.; Conde, O.; Minones, M.; Trillo, J. M.; Minones, J., Jr. Characterization of Poly(2-hydroxyethyl methacrylate) (PHEMA) Contact Lens using the Langmuir Monolayer Technique. *J. Colloid Interface Sci.* **2012**, *385*, 202.
- (44) Li, C.; Wang, B.; Liu, Y.; Cao, J.; Feng, T.; Chen, Y.; Luo, X. Synthesis and Evaluation of Star-shaped poly(-caprolactone)-poly(2-hydroxyethyl methacrylate) as Potential Anticancer Drug Delivery Carriers. *J. Biomater. Sci. Polym. Ed.* **2013**, *24*, 741.
- (45) Schramm, O. G.; Pavlov, G. M.; van Erp, H. P.; Meier, M. A. R.; Hoogenboom, R.; Schubert, U. S. A Versatile Approach to Unimolecular Water-Soluble Carriers: ATRP of PEGMA with Hydrophobic Star-Shaped Polymeric Core Molecules as an Alternative for PEGylation. *Macromolecules* **2009**, *42*, 1808.
- (46) Sheiko, S. S.; Borisov, O. V.; Prokhorova, S. A.; Moller, M. Cylindrical Molecular Brushes under Poor Solvent Conditions: Microscopic Observation and Scaling Analysis. *Eur. Phys. J. E. Soft Matter* **2004**, *13*, 125.
- (47) Han, D.; Tong, X.; Zhao, Y. One-Pot Synthesis of Brush Diblock Copolymers through Simultaneous ATRP and Click Coupling. *Macromolecules* **2011**, *44*, 5531.
- (48) Bareford, L. M.; Swaan, P. W. Endocytic Mechanisms for Targeted Drug Delivery. *Adv. Drug Delivery Rev.* **2007**, *59*, 748.
- (49) Soppimath, K. S.; Liu, L. H.; Seow, W. Y.; Liu, S. Q.; Powell, R.; Chan, P.; Yang, Y. Y. Multifunctional Core/Shell Nanoparticles Self-Assembled from pH-Induced Thermosensitive Polymers for Targeted Intracellular Anticancer Drug Delivery. *Adv. Funct. Mater.* **2007**, *17*, 355.
- (50) Zhang, Y.; Yang, Y.; Hong, H.; Cai, W. Multimodality Molecular Imaging of CD105 (Endoglin) Expression. *Int. J. Clin. Exp. Med.* **2011**, *4*, 32.
- (51) Alauddin, M. M. Positron Emission Tomography (PET) Imaging with  $^{18}\text{F}$ -based Radiotracers. *Am. J. Nucl. Med. Mol. Imaging* **2012**, *2*, 55.
- (52) Grassi, I.; Nanni, C.; Allegri, V.; Morigi, J. J.; Montini, G. C.; Castellucci, P.; Fanti, S. The Clinical use of PET with  $^{11}\text{C}$ -acetate. *Am. J. Nucl. Med. Mol. Imaging* **2012**, *2*, 33.
- (53) Fakhri, G. E. Ready for Prime Time? Dual Tracer PET and SPECT Imaging. *Am. J. Nucl. Med. Mol. Imaging* **2012**, *2*, 415.
- (54) Nolting, D. D.; Nickels, M. L.; Guo, N.; Pham, W. Molecular Imaging Probe Development: a Chemistry Perspective. *Am. J. Nucl. Med. Mol. Imaging* **2012**, *2*, 273.
- (55) van Dongen, G. A.; Ussi, A. E.; de Man, F. H.; Migliaccio, G. EATRIS, a European Initiative to Boost Translational Biomedical Research. *Am. J. Nucl. Med. Mol. Imaging* **2013**, *3*, 166.
- (56) Ravetch, J. V.; Bolland, S. IgG Fc receptors. *Annu. Rev. Immunol.* **2001**, *19*, 275.